Physics of Fluids

# Influence of reservoir properties on the dynamics of a migrating current of carbon dioxide EP

Cite as: Phys. Fluids **33**, 016602 (2021); https://doi.org/10.1063/5.0031632
Submitted: 02 October 2020 . Accepted: 17 December 2020 . Published Online: 08 January 2021

**Marco De Paoli**

## COLLECTIONS

Paper published as part of the special topic on Invited Contributions from Early Career Researchers 2020ECR2020

EP This paper was selected as an Editor's Pick

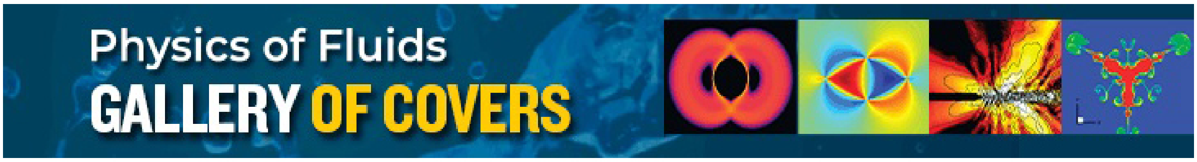

Physics of Fluids ARTICLE scitation.org/journal/phf

# Influence of reservoir properties on the dynamics of a migrating current of carbon dioxide

**Cite as: Phys. Fluids 33, 016602 (2021); doi: 10.1063/5.0031632**
**Submitted: 2 October 2020 • Accepted: 17 December 2020 •**
**Published Online: 8 January 2021**

View Online Export Citation CrossMark

**Marco De Paoli**[a)]

## AFFILIATIONS

Institute of Fluid Mechanics and Heat Transfer, TU Wien, Getreidemarkt 9, 1060 Vienna, Austria

**Note:** This paper is part of the Special Topic, Invited Contributions from Early Career Researchers 2020.
[a)]**Author to whom correspondence should be addressed:** marco.de.paoli@tuwien.ac.at

## ABSTRACT

Storage of carbon dioxide ($CO_2$) in saline aquifers is a promising tool to stabilize the anthropogenic $CO_2$ emissions. At the reservoir conditions, injected $CO_2$ is buoyant with respect to the ambient fluid (brine) and spreads as a current laterally and toward the top cap rock of the aquifer, with the potential risk of a leakage into the upper aquifer layers. However, $CO_2$ is partially soluble in brine and the resulting mixture ($CO_2$ + brine) is denser than both starting fluids. This heavy mixture makes the configuration unstable, producing a convective flow that enhances the dissolution of $CO_2$. Motivated by this geophysical problem, we analyze the influence of the porous medium properties on the evolution of a buoyant current that is weakly soluble with the ambient fluid. A time-dependent large-scale model [C. W. MacMinn *et al.*, "Spreading and convective dissolution of carbon dioxide in vertically confined, horizontal aquifers," Water Resour. Res. **48**, W11516 (2012)] is used to analyze the evolution of the flow. In this work, we include additional physical effects to this model, and we investigate the role of horizontal confinement, anisotropy, and dispersion of the porous layer in the dynamics of the fluid injected. The effect of anisotropy and dispersion is accounted by changing the dissolution rate of $CO_2$ in brine, which is obtained from experiments and Darcy simulations and represents a parameter for the model. Our results reveal that while the confinement has a remarkable effect on the long-term dynamics, i.e., on the lifetime of the current, anisotropic permeability and dispersion of the medium influence mainly the short-term behavior of the flow. Finally, we outline possible implications for the $CO_2$ sequestration process.

## I. INTRODUCTION

The global energy consumption has roughly doubled since 1970,[1] and most of the energy currently produced comes from the combustion of fossil fuels. As a result, the emissions of carbon dioxide ($CO_2$) increased dramatically in the last decades, with a consequent rise in the average temperature of the atmosphere. One possible solution to this global problem is represented by the carbon capture and storage (CCS) process. CCS consists of three phases: carbon dioxide produced from localized sources (e.g., power or industrial plants) is captured, pressurized to reach a liquid state, and finally injected in underground geological formations.[2,3] It is estimated that CCS can operate at least 100 years to stabilize the $CO_2$ emissions as a unique storage technology.[4] However, the process of $CO_2$ storage is made complex by the interaction of $CO_2$ with the ambient fluid and rocks, and it is currently subject of active investigations.[5] In this work, we analyze the influence of the reservoir properties on the evolution of the $CO_2$ current. We used an existing large-scale model[6,7] to study the dynamics of $CO_2$ after injection, and we include additional physical effects to investigate the role of horizontal confinement, anisotropy, and dispersion of the porous layer in the dynamics of the fluid injected.

We consider the process of carbon sequestration in saline aquifers, i.e., geological formations located 1–3 km beneath the earth surface.[8] The formation, sketched in Fig. 1, consists of a porous region bounded by two horizontal low-permeability layers. The horizontal extension of the formation (order of kilometers) is usually much larger than the distance between the impermeable layers (tens of meters). This configuration is typical of a layered site, e.g., the Sleipner Formation in the North Sea.[9] The aquifer, consisting of rock grains of different size (porous matrix), is initially saturated with ambient fluid [brine, yellow layer in Fig. 1(a)], i.e., highly salted water. When liquid-like $CO_2$ [black fluid in Fig. 1(a), density ≈ 500 kg/m$^3$] is injected in the aquifer, it is lighter than brine (density ≈ 1000 kg/m$^3$), and therefore, it migrates to occupy the upper portion of the porous layer. This effect is particularly undesired because in case of fractures of the top impermeable layer, $CO_2$ may eventually return to the atmosphere. On the other hand, during the process of migration from the injection point to the upper portion of the layer, $CO_2$ and brine interact along the interface between the two fluids and a mixture of $CO_2$ and brine forms [$CO_2$ + brine, red fluid in Fig. 1(a), density ≈ 1030 kg/m$^3$]. This fluid, which is heavier than both $CO_2$ and brine, deposits at the bottom of the formation, making $CO_2$ stable and safely stored. This mechanism, defined as solubility trapping, prevents $CO_2$ from leaking in case of fractures in the impermeable upper layer. The scenario described above is far from the assumptions behind the classical model of gravity current (immiscible fluids, absence of dispersion, and unconfined domain). This system should be considered as a current of buoyant fluid ($CO_2$) partially soluble in the ambient fluid (brine). Moreover, the current of the denser mixture ($CO_2$ + brine) that forms sinks, stabilizing the fluid to trap, but also interacts with the buoyant current, reducing the dissolution of the buoyant fluid.

Recent works[6,7] investigated the post-injection evolution of carbon dioxide currents, trying to predict the time taken to dissolve the amount of $CO_2$ injected in brine, i.e., evaluating the efficiency of the solubility trapping mechanism. We will use the models developed in these works and include additional physics to investigate the effects of the porous media properties on the evolution of the currents. The fluid mechanics of the mixing process can be split in three parts according to the scale of the flow structures involved, consisting of (i) large scale, (ii) Darcy scale, and (iii) pore scale. Each scale presents different flow dynamics, with different characteristic length and time scales, but all scales are closely connected to each other. The large-scale dynamics [Fig. 1(a)] is controlled by convection since the dominant driving force consists of the buoyancy induced by the density contrast between $CO_2$ and brine. At the interface between the currents of $CO_2$ and brine [Darcy scale, Fig. 1(b)], in turn, the process is controlled by diffusion and mixing. $CO_2$ dissolves in brine, and a layer of $CO_2$-rich mixture forms at the interface between the two fluids. When this layer is sufficiently thick, it becomes unstable and finger-like structures form[10] and control the subsequent evolution of the interfacial flow, ruling also the mixing of $CO_2$ in brine. The presence of these convective structures promotes the mixing of the two fluids, but the dissolution process may also be locally inhibited where the domain is saturated with $CO_2$. The dissolution dynamics influences the large-scale flow due to the change in the volume of the $CO_2$ layer and because of the interaction of the $CO_2$ current with the current of $CO_2$ + brine. Finally, at the pore-scale [Fig. 1(c)], the fluid flows through the rock grains following sinuous paths. If, as in this case, a solute ($CO_2$) is transported by the fluid, the tortuous fluid trajectory will produce additional spreading of solute. This mechanism, labeled dispersion, influences directly the dissolution dynamics of the flow at the Darcy scale and therefore also the dynamics at the larger scales. The behavior of this multiscale mixing process is hard to study, also due to the large computational cost required to resolve all the scales of the flow. Therefore, the problem is tackled separately at different levels to account for the effects of buoyancy (large-scale), dissolution (Darcy scale), and dispersion (pore-scale).

In this work, we consider the trapping mechanism of $CO_2$ induced by convective mixing and we investigate the role of the domain properties in the evolution of the flow. First, we will analyze the effect of the domain size, in particular of the lateral confinement, on the lifetime of the current. Indeed, geological formations cannot be considered as horizontal unconfined layers due to the orientation and shape of the impermeable layers. Then, we will consider the effect of anisotropy of the medium. Although the rock structure is usually considered as an isotropic porous matrix, formations identified as possible sequestration sites may be of sedimentary origin,

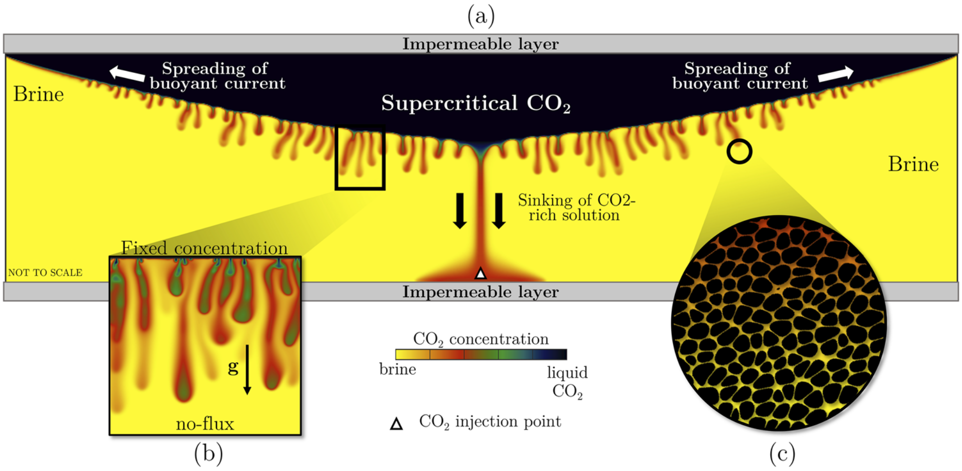

**FIG. 1.** Evolution of a carbon dioxide current: post-injection scenario. (a) Large-scale dynamics. Interaction of the injected carbon dioxide (black) and brine (yellow). After injection, carbon dioxide tends to spread and occupy the upper portion of the domain. (b) Darcy-scale dynamics. During the spreading process, dissolution of $CO_2$ in brine takes place and a mixture heavier than brine (red) forms. This dissolution mechanism makes the interface between the two fluids to be unstable, and finger-like structures form. (c) Pore-scale dynamics. The reservoir is made of small grains of different size, which produce additional spreading of $CO_2$, eventually influencing the dissolution mechanism.

i.e., obtained as the deposition of subsequent layers.[11,12] As a result of this formation process, the properties of the porous matrix in the horizontal and vertical direction may differ, which makes the formation behavior anisotropic. Finally, the effect of dispersion will be analyzed: the presence of the rock grains produces a modification of the local $CO_2$ concentration gradients, and this effect will influence the dissolution rate. We will use a large-scale model[6,7] developed in the context of isotropic and horizontally unconfined layers in the absence of dispersion, and we will include additional physical effects to investigate the role of the domain with the anisotropy and dispersion of the porous domain in the lifetime of a $CO_2$ current. We describe the evolution and dynamics of the currents in Sec. II. Problem formulation and governing equations are presented in Sec. III. Finally, results and possible implications for carbon sequestration are presented in Secs. IV and V, respectively.

## II. DYNAMICS OF GRAVITY CURRENTS

We discuss here the process of mixing and dissolution at three different flow scales, which are closely interconnected. The flow at these scales, namely, large scale (Sec. II A), Darcy scale (Sec. II B), and pore scale (Sec. II C), is controlled by buoyancy, solutal convection, and solute dispersion, respectively.

### A. Large-scale dynamics and the effect of buoyancy

We consider a rectangular, porous domain confined by two horizontal and impermeable layers. The system is represented in Fig. 2. The domain is initially saturated with brine (yellow fluid), and a volume of $CO_2$ is injected (black fluid) in the center of the layer. Due to symmetry, we only consider the right portion of the domain [Fig. 2(a)]. The flow is initially driven by buoyancy, which is induced by the large density contrast ($\approx 500\ \mathrm{kg/m^3}$) between $CO_2$ and brine. This makes the $CO_2$ to form a current that migrates to occupy the upper portion of the layer [Fig. 2(b)].

The migration process is characterized by the dissolution of $CO_2$ at the interface between the layer of $CO_2$ and pure brine, where a heavier solution of $CO_2$ + brine forms. The interface is therefore unstable, and small convective instabilities, labeled fingers, form [Figs. 2(c)–2(e)]. Fingers promote the dissolution of $CO_2$ in brine, which is a highly desirable effect since it contributes to the permanent trapping of $CO_2$. The presence of these structures has two main effects on the flow: the volume of the $CO_2$ current diminishes and a second current of heavy mixture ($CO_2$ + brine, red fluid in Fig. 2) forms. This $CO_2$ + brine current, defined by the portion of the domain characterized by the high concentration of $CO_2$ [region delimited by red lines in Figs. 2(c)–2(g)], also has a strong influence on the dissolution process: when the interfacial region between the two currents is saturated with $CO_2$, dissolution is considerably slowed down. This phenomenon, also labeled shutdown of convection,[10,13,14] has been studied in detail via numerical simulations and will be further discussed in Sec. II B.

The impact of domain saturation is remarkable, in particular on the lifetime of the $CO_2$ current.[6] The dissolution rate will considerably reduce, and the mixing process may almost arrest. In this stage, the current of $CO_2$ will continue to spread and the dynamics will be again mainly controlled by buoyancy. Finally, for sufficiently long times, the volume of $CO_2$ initially injected will completely dissolve [Fig. 2(h)]. The time taken to achieve this condition is extremely important since it can be used to quantify the efficiency of the trapping mechanism in the specific configuration of the reservoir considered. We wish to remark here that the domain width can influence the evolution of both the $CO_2$ and the $CO_2$ + brine currents. Indeed, when the current of a heavy mixture reaches the domain boundaries ($x^* = L^*$) and cannot grow further horizontally, it grows vertically and the portion of the interface effective for dissolution [blue line in Figs. 2(f)–2(g)] reduces further.

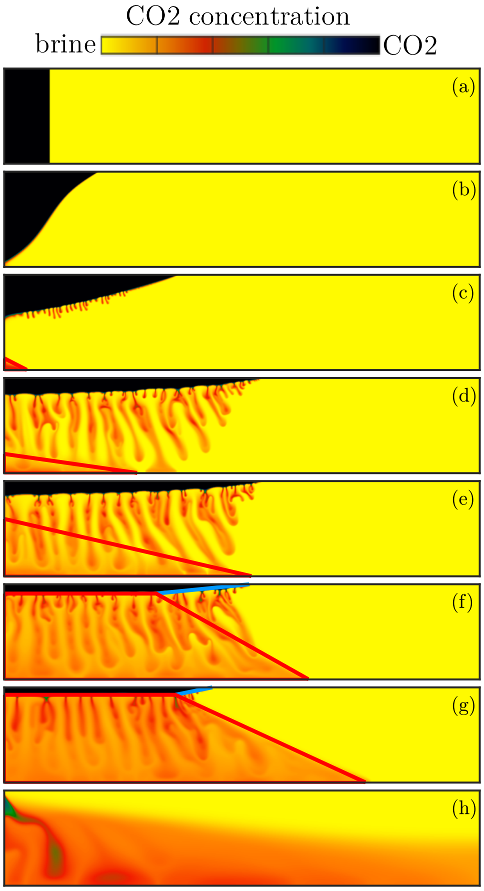

**FIG. 2.** Process of carbon dioxide spreading and dissolution in geological formations. Time-dependent $CO_2$ concentration distribution is shown. Time advances from (a) to (h). Concentration fields obtained via numerical simulations (numerical details are available in Refs.15 and 16). Boundaries of the $CO_2$ + brine current are also shown [red lines in (c)–(g)]. After contact of the two currents, dissolution can only take place along the interface between $CO_2$ and pure brine [blue lines in (f) and (g)].

This system has been modeled by MacMinn *et al.*[6] in the instance of unconfined and isotropic geological formations, in the absence of dispersion. They observed that the growth of the heavy fluid current can considerably slow down this dissolution mechanism, reducing the efficiency of the solubility trapping. In this work, we will use the same model to include additional physical effects, and we will analyze the effect of porous medium properties on the evolution of the $CO_2$ current. The dynamics at the interface of the two currents, where the dissolution takes place, is described in Sec. II B. We will include the effect of domain anisotropy and solute dispersion modeling the solute dissolution rate at the interface of the currents.

### B. Darcy-scale and interfacial dynamics

One of the key parameters influencing the evolution of the two-current system is represented by the $CO_2$ dissolution rate at the interface of the $CO_2$ and brine currents. As discussed above, dissolution is promoted by the action of finger-like structures, which considerably increase the rate of mixing with respect to the case of a flat interface.[17] On the other hand, the non-linear dynamics of these structures, which interact, split, and merge in a complex fashion, makes predictions hard to obtain.[18] The mixing process at the interface of the two currents is usually studied in rectangular domains [Fig. 1(b)], where the concentration of the $CO_2$ + brine mixture is assumed constant along the top boundary, whereas the no-flux boundary condition is applied along the bottom wall. This configuration has been analyzed in detail in a number of numerical[10,13,19,20] and experimental works,[18,19,21–24] and accurate scaling laws for the dissolution rate of $CO_2$ in brine have been derived for isotropic and homogeneous,[13,15] anisotropic[14,25–27] and heterogeneous[25,28,29] porous media. We refer to Ref. 30 for a comprehensive review on the topic. In the following, we briefly recall the governing equations and the main features of the dissolution dynamics.

The process of convective dissolution may be investigated at an intermediate length scale, comprised between the characteristic length scale of the domain (the domain height, $H^*$) and the pore-scale (the average pore diameter, $d^*$). At this level, the flow in each phase $i$ is considered incompressible, and continuity applies,

$$\nabla \cdot \mathbf{u}_\mathbf{i}^* = 0. \tag{1}$$

Moreover, momentum transport is controlled by the Darcy law, in which the Darcy velocity of the phase ($\mathbf{u}_\mathbf{i}^*$) is proportional to the local pressure ($p^*$) gradient, as follows:

$$\mathbf{u}_\mathbf{i}^* = \frac{1}{\mu_i}\mathbf{K}\left(-\nabla p_i^* + \rho_i \mathbf{g}\right), \tag{2}$$

where $\mu_b$ is the viscosity of the phase considered, $\mathbf{K}$ is the permeability tensor, $\rho_i$ is the local fluid density, and $\mathbf{g}$ is acceleration due to gravity. We use here the symbol $^*$ to refer to dimensional variables. In this frame, the Oberbeck–Boussinesq approximation applies.[31] The solute concentration ($C^*$) is governed by the advection–dispersion equation,

$$\phi\frac{\partial C^*}{\partial t^*} + \mathbf{u}_\mathbf{i}^* \cdot \nabla C^* = \phi \nabla \cdot \left[\mathbf{D}(\mathbf{u}_\mathbf{i}^*) \cdot \nabla C^*\right], \tag{3}$$

where $\phi$ is the porosity and the dispersion tensor, $\mathbf{D}(\mathbf{u}^*)$, accounts for the effect of solute dispersion induced by the presence of the obstacles (rock grains) of the porous matrix. Dispersion has remarkable effects on the onset[32,33] and the subsequent development of convection,[34] as well as on the dissolution rate.[24,35] However, to provide an expression for the dispersion tensor $\mathbf{D}(\mathbf{u}^*)$, accurate pore-scale analyses of convective flows should be performed, which will be discussed in Sec. II C.

### C. Pore-scale dynamics and the effect of dispersion

As the fluid flows through the porous matrix, the fluid particles continually change direction due to the presence of the rock grains, leading to a random-walk-type process in which individual particles gradually spread and cause mixing of solute.[36] This phenomenon, defined as (mechanical) dispersion, may be interpreted as follows. We consider a patch of dyed fluid spreading out as it moves in a uniform downward flow through a bead pack. The dye spreads over a considerable region in the flow direction, and this effect, defined as longitudinal dispersion, is measured via the longitudinal dispersivity coefficient, $\alpha_l$. The presence of the grains will also induce a lateral spreading, i.e., in the direction perpendicular to the flow, which is quantified by the transverse dispersivity coefficient, $\alpha_t$. The relative importance of these two contributions is defined by the dispersivity ratio, $r = \alpha_l/\alpha_t$, normally $r \gg 1$ for geological applications, in which longitudinal dispersion dominates. However, the presence of transverse dispersion produces a modification of the flow structure[35] and of the dissolution mechanisms,[23] and therefore, it should be taken into account to define the dissolution rate.

Dispersion has been identified[23,24,37,38] as possible responsible of the discrepancy in the numerical and experimental measurements of the dissolution rate, and therefore, it represents a very active topic of research. Since dispersion is due to nonuniformities of the flow at the level of the grains, pore-scale simulations and experiments have been used to investigate the phenomenon, in an attempt to derive dispersion models to include in simulations at the Darcy scale. A variety of approaches have been proposed to model the effect of solute dispersion. Sardina *et al.*[39] performed direct numerical simulations to investigate the flow through an array of spheres and developed a model to include the effect of dispersion as a drag term in the Navier–Stokes equations. Experimental[40] and numerical[41] measurements in natural convection in porous media have shown that the flow structure and the dissolution rate are determined by the ratio of the thermal length scale (boundary layer thickness) to the porous length scale (average grain size). In addition, Gasow *et al.*[38] demonstrated, with the aid of pore-scale numerical simulations, that the pore size should be used as the characteristic length when the dispersion term is modeled. The boundary layer thickness is set by the pore size, and the porosity also has a strong influence on the dissolution rate. The same conclusions are supported by the numerical work of Liu *et al.*,[42] where the pore size is still identified as an important factor to determine the dissolution rate. Feixiong, Kuznetsov, and Jin[43] used pore-scale simulations to investigate the effect of momentum dispersion. They proposed a model based on the effective fluid viscosity, and they have shown that this approach is valid for a wide range of porosity values.

In this work, we include the effect of dispersion modeling the dissolution rate at the Darcy scale. We adopted the model proposed by Wen, Chang, and Hesse,[35] which is based on both experimental observations[24] and numerical simulations.[35] Further details are provided in Sec. III B.

## III. METHODOLOGY

### A. Derivation of the large-scale model

In this section, we present the system configuration and we derive the large-scale model, which has already been used in previous studies in the instance of isotropic domains in absence of dispersion.[6,44,45] We consider a rectangular domain of extension $2L^*$ and $H^*$ in the horizontal ($x^*$) and vertical ($z^*$) directions, respectively (the superscript $^*$ is used here to refer to dimensional variables). This two-dimensional configuration is motivated by the injection scenario consisting of a linear array of wells. The system is sketched in Fig. 3, and due to symmetry, only the right part of the domain ($x^* \geq 0$) is considered. Initially, the domain is saturated with brine [yellow fluid in Fig. 3(a), density $\rho_w$ and viscosity $\mu_w$]. We assume that the system is homogeneous and characterized by uniform porosity ($\phi$) and anisotropic permeability ($k_v$ and $k_h$ in the vertical and horizontal directions, respectively). At time $t^* = 0$, a volume $2L_0^* \times H^*$ of $CO_2$ [black fluid in Fig. 3(a), density $\rho_c$ and viscosity $\mu_c$] is injected in the central portion of the domain, characterized by $-L_0^* \leq x^* \leq L_0^*$ and $0 \leq z^* \leq H^*$ [Fig. 3(a)].

We briefly derive here the one-dimensional large-scale model adopted (see Refs. 46 and 47 for a detailed derivation of the equations). We assume that the domain is homogeneous, with constant porosity $\phi$ and with the permeability field uniform and anisotropic, i.e., the permeability tensor introduced in Eq. (2) is defined as

$$\mathbf{K} = \begin{bmatrix} k_h & 0 \\ 0 & k_v \end{bmatrix}, \tag{4}$$

with $k_h$ and $k_v$ permeability values in the horizontal and vertical directions, respectively. We also consider the domain two-dimensional and characterized by a small aspect ratio ($H^* \ll L^*$). In this configuration, we consider the fluids as three distinct regions of uniform density and viscosity and the Darcy equation (2) applies to each phase $i$,

$$\mathbf{u_i^*} = \begin{bmatrix} u_i^* \\ w_i^* \end{bmatrix} = \frac{1}{\mu_i}\mathbf{K}\left(-\nabla p_i^* + \rho_i \mathbf{g}\right), \tag{5}$$

where $i$ stands for $c$ ($CO_2$ phase), $w$ (brine phase), and $m$ ($CO_2$ + brine phase). Since $H^* \ll L^*$, the vertical velocity component $w_i^*$ is negligible with respect to the horizontal one, $u_i^*$, and the $z$ component of Eq. (5) suggests that the pressure $p_i^*(x^*, z^*, t^*)$ in each phase is hydrostatic. When expressed as a function of the pressure at the interface between the currents of $CO_2$ and brine, $p_0^*(x, t)$, the pressure in each fluid phase reads

$$p_c^*(x^*, z^*, t^*) = p_0^*(x^*, t^*) + \rho_c g(H^* - h^* - z^*), \tag{6}$$

$$p_w^*(x^*, z^*, t^*) = p_0^*(x^*, t^*) + \rho_w g(H^* - h^* - z^*), \tag{7}$$

$$p_m^*(x^*, z^*, t^*) = p_0^*(x^*, t^*) + \rho_w g h_m^* + \rho_m g(h_m^* - z^*), \tag{8}$$

with $h_i^*$ being the thickness of the currents, as indicated in Fig. 3. For all locations $x^*$, the height of the fluid layer is obtained as the sum of the thicknesses of each fluid phase,

$$h_c^*(x^*, t^*) + h_w^*(x^*, t^*) + h_m^*(x^*, t^*) = H^*. \tag{9}$$

Moreover, since the flow is assumed to be incompressible, volume conservation is guaranteed along the domain,

$$\int_0^{h_m^*} u_m^* \, \mathrm{d}z + \int_{h_m^*}^{h_m^*+h_w^*} u_b^* \, \mathrm{d}z + \int_{h_m^*+h_w^*}^{H^*} u_c^* \, \mathrm{d}z = 0. \tag{10}$$

On the other hand, one can write the local equation for the conservation of mass in the currents of $CO_2$ and $CO_2$ + brine mixture, respectively,

$$\phi \frac{\partial h^*}{\partial t^*} = -\frac{\partial}{\partial x^*}\left[\int_{h_m^*+h_w^*}^{H^*} u_c^* \, \mathrm{d}z\right] - q_m^*, \tag{11}$$

$$\phi \frac{\partial h_m^*}{\partial t^*} = -\frac{\partial}{\partial x^*}\left[\int_0^{h_m^*} u_m^* \, \mathrm{d}z\right] + \frac{q_m^*}{X_v}, \tag{12}$$

where we introduced the volume of $CO_2$ dissolved in brine per unit of $CO_2$-brine interface and time, $q_m^*$ $[\mathrm{m}^3/(\mathrm{m}^2\mathrm{s})]$. We also used the volume fraction of $CO_2$ in the $CO_2$ + brine mixture, $X_v = \rho_m X_m / \rho_c$, $X_m$ being the correspondent mass fraction. As described in Sec. II, the role of the current of the $CO_2$ + brine mixture is crucial since it can dramatically inhibit the dissolution of $CO_2$ in brine, considerably increasing the time required to achieve a complete dissolution. To account for the interaction of the current of heavy fluid with the current of buoyant fluid, the dissolution rate $q_m^*$ is defined locally so that there is no dissolution along the interface in which the currents of $CO_2$ and $CO_2$ + brine are in contact, i.e., when $h^*(x) + h_m^*(x) = H^*$ [red interface in Fig. 3(c)], whereas the dissolution can take place with rate $q_m^*$ where the currents of brine and $CO_2$ are in contact [blue interface in Fig. 3(c)].

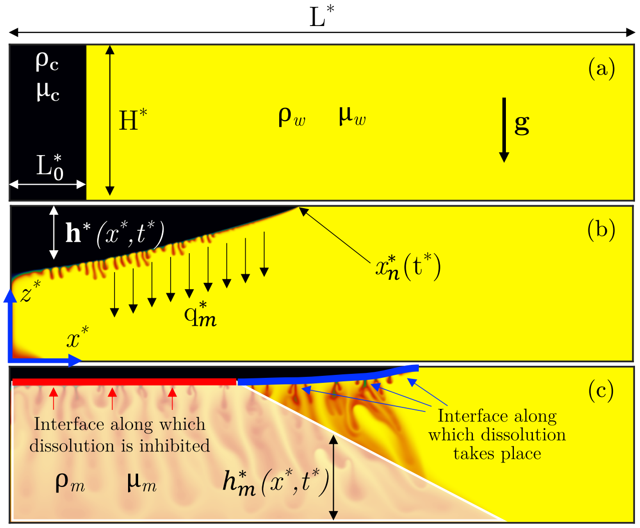

**FIG. 3.** Sketch of the flow configuration. (a) Initial condition: $CO_2$ (black fluid, $\rho_c$, $\mu_c$) is injected and is initially surrounded by brine (yellow fluid, $\rho_w$, $\mu_w$). (b) Buoyant current is defined by the layer height, $h^*(x^*, t^*)$, and current nose, $x_n^*(t^*)$, i.e., the maximum horizontal extension of the $CO_2$ current. At the interface between $CO_2$ and brine, $CO_2$ dissolves and a downward flux ($q_m^*$) generates a third current of heavy fluid ($CO_2$ + brine, red fluid, $\rho_m$, $\mu_m$). (c) When the currents of $CO_2$-rich mixture and brine are in contact, dissolution is inhibited (red interface). The dissolution process continues along the portion of the interface between $CO_2$ and brine (blue interface). $CO_2$-rich current is described by its height, $h_m^*(x^*, t^*)$.

Equations (11) and (12), which control the evolution of the currents, can be solved by taking the horizontal velocity components from Eq. (5). The pressure gradients are computed from Eqs. (6)–(8), in which $p_0^*(x^*, t^*)$ is obtained from volume conservation (10). Finally, $h_w^*$ is expressed as a function of $h_m^*$ and $h_c^*$ using Eq. (9), and Eqs. (11) and (12) reduce to the form

$$\phi\frac{\partial h^*}{\partial t^*} - \frac{\phi}{\gamma}\frac{\partial}{\partial x^*}\left[W^*(1-f)h^*\frac{\partial h^*}{\partial x^*} - W_m^* f h_m^*\frac{\partial h_m^*}{\partial x^*}\right] = -q_m^*, \tag{13}$$

$$\phi\frac{\partial h_m^*}{\partial t^*} - \frac{\phi}{\gamma}\frac{\partial}{\partial x^*}\left[W_m^*(1-f_m)h_m^*\frac{\partial h_m^*}{\partial x^*} - W^* f_m h^*\frac{\partial h^*}{\partial x^*}\right] = \frac{q_m^*}{X_v}, \tag{14}$$

where $W^* = (\rho_w - \rho_c)gk_v/\phi\mu_c$ is the $CO_2$ buoyancy velocity, $W_m^* = (\rho_m - \rho_w)gk_v/\phi\mu_c$ is the mixture buoyancy velocity, $\gamma = k_v/k_h$ is the permeability ratio, and $g$ is the acceleration due to gravity. We finally define the functions $f$ and $f_m$, employed in Eqs. (13) and (14), as

$$f = \frac{Mh^*/H^*}{(M-1)h^*/H^* + (M_m-1)h_m^*/H^* + 1}, \tag{15}$$

$$f_m = \frac{M_m h_m^*/H^*}{(M-1)h^*/H^* + (M_m-1)h_m^*/H^* + 1}, \tag{16}$$

where $M = \mu_w/\mu_c$ and $M_m = \mu_w/\mu_m$ stand for the mobility ratio of the buoyant and dense current, respectively.

#### *1. Dimensionless equations*

Equations (13) and (14) fully describe the evolution of the currents of $CO_2$ and $CO_2$ + brine, in the presence of dissolution. To make the equations dimensionless, we rescale variable as follows. A natural reference scale for the current's thickness is the layer height, $H^*$. For the horizontal coordinate, we set as reference length scale $L_0/\sqrt{\gamma}$, i.e., the initial width of the $CO_2$ current corrected by the effect of the anisotropy ratio, $\gamma = k_v/k_h$. Finally, we choose as reference time scale $T^* = (L_0^*)^2/(W^*H^*)$. As a result, dimensionless variables are obtained as

$$h = \frac{h^*}{H^*}, \quad h_m = \frac{h_m^*}{H^*}, \tag{17}$$

$$x = \frac{x^*}{L_0^*/\sqrt{\gamma}}, \quad t = \frac{t^*}{(L_0^*)^2/(W^*H^*)}. \tag{18}$$

We define the buoyancy velocity ratio $\delta = W_m^*/W^*$, i.e., the ratio between the buoyancy velocities computed with respect to mixture–brine and brine–$CO_2$. With this set of variables, the two-current system is controlled by the following dimensionless equations:

$$\frac{\partial h}{\partial t} - \frac{\partial}{\partial x}\left[(1-f)h\frac{\partial h}{\partial x} - \delta f h_m\frac{\partial h_m}{\partial x}\right] = -\varepsilon_0, \tag{19}$$

$$\frac{\partial h_m}{\partial t} - \frac{\partial}{\partial x}\left[\delta(1-f_m)h_m\frac{\partial h_m}{\partial x} - f_m h\frac{\partial h}{\partial x}\right] = \frac{\varepsilon_0}{X_v}, \tag{20}$$

where we introduced the volume fraction of $CO_2$ in the $CO_2$ + brine mixture, $X_v = \rho_m X_m/\rho_c$, $X_m$ being the correspondent mass fraction. To take into account the presence of the second current that inhibits the dissolution along the $CO_2$ + brine interface, the dissolution rate $\varepsilon$ is defined as follows:

$$\varepsilon_0(x) = \begin{cases} 0 & \text{if} \quad h(x) = 0 \text{ or } h(x) + h_m(x) = 1 \\ \varepsilon & \text{else,} \end{cases} \tag{21}$$

with

$$\varepsilon = \frac{q_m^*}{\phi W^*}\left(\frac{L_0^*}{H^*}\right)^2. \tag{22}$$

The parameter $\varepsilon$ will be defined in detail in each specific configuration considered. Definition (21) suggests that dissolution is inhibited when the light fluid is absent [i.e., $h(x) = 0$] or the two currents touch [$h(x) + h_m(x) = 1$].

In the following, we define the parameters used for the porous medium, fluids, and dissolution rate.

### B. Physical and dimensionless parameters

The two-current model described by Eqs. (19) and (20) is sensitive to the domain properties and to the fluid properties. We study three different injection scenarios consisting of variable domain size, permeability ratio, and transverse dispersion. The set of parameters used is summarized in Table I for all simulations considered and is obtained as follows.

#### *1. Domain properties*

We consider an aquifer in the Frio C Formation (Texas, US).[48] This formation is characterized by a layer thickness $H^* = 7$ m, porosity $\phi = 0.3$, and permeability $k_v = 2 \times 10^{-12}$ m$^2$. We consider the initial horizontal extension of the volume of $CO_2$ injected $L_0^*$

**TABLE I.** Summary of dimensionless parameters used for the simulations. Effects of domain size (S1), anisotropy of the medium (S2), and dispersion (S3) are studied. Physical parameters are reported in Sec. III B.

| | Domain properties | | | Fluid properties | | | | Dissolution properties | |
|---|---|---|---|---|---|---|---|---|---|
| No. | $\gamma$ | $\Delta$ | $L$ | $M$ | $M_m$ | $\delta$ | $X_v$ | $Ra$ | $\varepsilon$ |
| S1 | 1 | $\infty$ | 50–140 | 1 | 1 | 0.02 | 0.02 | $2.4 \times 10^3$ | $10^{-5}$ |
| S2 | 1/8-1 | $\infty$ | 140 | 1 | 1 | 0.02 | 0.02 | $2.4 \times 10^3$ | $10^{-5}\gamma^{-1/2}$ |
| S3 | 1 | $5 \times 10^{-3}$–$5 \times 10^5$ | 140 | 1 | 1 | 0.02 | 0.02 | $2.4 \times 10^3$ | $\varepsilon(\Delta)$ [Fig. 4(a)] |

= 14 m. A further parameter to be taken into account is the domain extension in the horizontal direction, $L^*$. Indeed, porous layers can hardly be considered as infinitely extended in the horizontal direction but should rather be modeled as finite-width regions. This is due to the irregular shape of the impermeable layers that divide adjacent regions of the reservoir. For instance, the morphology of the Sleipner Site in the North Sea has been studied in detail via seismic images.[49–51] These measurements indicate that the layer shape is irregular, with nearly horizontal layers bounded by inclined walls. We decide to model this effect by adding a lateral confinement to the geometry considered. We considered a wide range of horizontal domain size, $L^*$. The correspondent dimensionless extension $L$, normalized with $L_0^*$, is indicated in Table I for all cases considered. In Appendix A, we report a list of parameters relative to geological formations identified as possible sequestration sites.

### *2. Fluid properties*

The viscosity and density of CO$_2$ and brine are obtained from Ref. 52. These parameters are sensitive to temperature and pressure and vary with the depth of the reservoir. Further details are provided in Appendix A. CO$_2$ density and viscosity are assumed to be $\rho_c = 700$ kg/m$^3$ and $\mu_c = 6 \times 10^{-5}$ Pa s, respectively, whereas brine density and viscosity are $\rho_w = 945$ kg/m$^3$ and $\mu_c = 2 \times 10^{-4}$ Pa s.[53] We assume that the viscosity of the mixture does not change significantly with respect to brine[6] ($\mu_m = \mu_w$) and the density difference existing between brine and CO$_2$ + brine mixture is[53] $\rho_m - \rho_w = 10.45$ kg/m$^3$. Moreover, a mass fraction of fluid mixture dissolved in brine $X_m = 0.01$ is considered,[6] and the corresponding volume fraction is $X_v \approx 0.02$. According to the above-mentioned properties, we obtain velocity ratio $\delta \approx 0.02$ and mobility values $M_m = 1$ and $M \approx 3$. The large value of $M$ (that might be even larger, up to 10 times, see Appendix A) can be responsible for the formation of very elongated CO$_2$ plumes, which might change considerably the dynamics of the current with respect to the cases $M < 1$.[54] For simplicity, in the present work, we assume $M = M_m = 1$, which gives $f = h$ and $f_m = h_m$.

### *3. Dissolution parameters*

The estimated dissolution rate, $q_m^*$ [m$^3$/m$^2 s$], is the volume of CO$_2$ dissolved per unit of CO$_2$–brine interface area and time. It depends on the porous medium properties, fluid properties, and flow conditions, and a precise estimate is hard to obtain. As discussed in Sec. II B, a series of studies investigated the role of these properties in the flux of CO$_2$ dissolved in different flow configurations and porous medium properties. These studies considered the effect of convection via two-dimensional simulations and experiments, usually in rectangular geometries, and provide measurements of the amount (mass) of saturated CO$_2$ + brine solution mixed in brine per unit of mixture–brine interfacial area and time.[10,23,53] For instance, for homogeneous and isotropic porous media, the dissolution rate of a CO$_2$-saturated solution in brine is $\mathscr{F}^*$,

$$\mathscr{F}^* = \mathscr{F} W_m^* C_{sat}^* , \tag{23}$$

with $\mathscr{F}$ being the dimensionless dissolution rate. While measurements in two-dimensional simulations[10,13,14,53] suggest that $\mathscr{F} = 0.017$, experiments[19,23] show that $\mathscr{F}$ could be up to ten times higher, and in this work, we assume $\mathscr{F} = 0.14$. Since the concentration of CO$_2$ in brine is up to 3 wt. % at the reservoir conditions,[8] we have that $C_{sat}^* \approx 29$ kg/m$^3$. With the set of parameters considered, we obtain $\mathscr{F}^* \approx 1.4 \times 10^{-5}$ kg/m$^2$ s, corresponding to $q_m^* = \mathscr{F}^* X_v/\rho_m \approx 2 \times 10^{-10}$ m$^3$/m$^2$ s. Finally, from Eq. (22), we obtain the dimensionless dissolution rate $\varepsilon \approx 10^{-5}$. We set this value of $\varepsilon$ as reference for an isotropic medium in the absence of dispersion, and we analyze the effect of anisotropy and dispersion as follows.

*a. Effect of anisotropy.* We take into account the effect of the anisotropy ratio of the porous medium $\gamma = k_v/k_h$, i.e., the ratio of vertical ($k_v$) to horizontal ($k_h$) permeability. In anisotropic media, the resistance experienced by the fluid to flow in the horizontal and vertical directions is different. This is the case of sedimentary formations, in which the reservoir is obtained as a result of the deposition of subsequent layers, giving different properties (e.g., permeability) in different directions. For cases of practical interest, it is observed[11] that $\gamma$ can be as small as 0.1.[12] Green and Ennis-King[25] have shown that in two-dimensional domains at low and intermediate Rayleigh numbers, the dissolution rate of an anisotropic porous medium, $\varepsilon(\gamma)$, can be defined as a function of the dissolution rate in an isotropic porous medium having the same vertical permeability, $\varepsilon(\gamma = 1)$, as follows:

$$\varepsilon(\gamma) = \varepsilon(\gamma = 1)\gamma^{-1/2} , \tag{24}$$

with $1/20 \le \gamma \le 1$. It was later shown that Eq. (24) is still valid at high Rayleigh numbers[14] (up to $Ra = 2 \times 10^4$) and in three-dimensional domains.[27] In this work, we will analyze the effect of anisotropy by changing the parameter $\gamma$ and correspondingly the dissolution rate $\varepsilon$ according to Eq. (24).

*b. Effect of dispersion.* The effect of dispersion plays an important role in the dissolution dynamics.[32,33] This effect has been quantified systemically with the aid of Darcy simulations,[35] and it was shown that the dissolution rate is the result of the combined action of convection, diffusion, and dispersion. The relative role of convection and diffusion is accounted by the Rayleigh–Darcy number $Ra$,

$$Ra = \frac{W_m^* H}{D} , \tag{25}$$

with molecular diffusion coefficient $D \approx 10^{-9}$ m$^2$/s.[33] The effect of dispersion is quantified[24] by the ratio of molecular and transverse dispersion coefficients, $\Delta = D/D_t$, where the transverse dispersion coefficient, $D_t = W_m \alpha_t$, depends on the transverse dispersivity, $\alpha_t$ (see Sec. II C). When $\Delta \ll 1$, transverse dispersion dominates, and when $\Delta \gg 1$, molecular diffusion dominates.

Wen, Chang, and Hesse[35] analyzed an isotropic system at $Ra = 2 \times 10^4$ and dispersivity ratio $r = 10$, i.e., within the same range of parameters considered in this study ($Ra = 24 \times 10^3$ and $r = 10$). They computed the dissolution rate of the system for a wide range of $\Delta$. In particular, we show in Fig. 4(a) the normalized dissolution rate $\varepsilon(\Delta)/\varepsilon(\Delta \to \infty)$ (solid line), i.e., the dissolution rate for a given $\Delta$, $\varepsilon(\Delta)$, divided by the dissolution rate in the absence of dispersion, $\varepsilon(\Delta \to \infty)$. The non-monotonic behavior of the dissolution rate obtained from Ref. 35 is explained by analyzing the structure of the flow. When convection dominates over dispersion

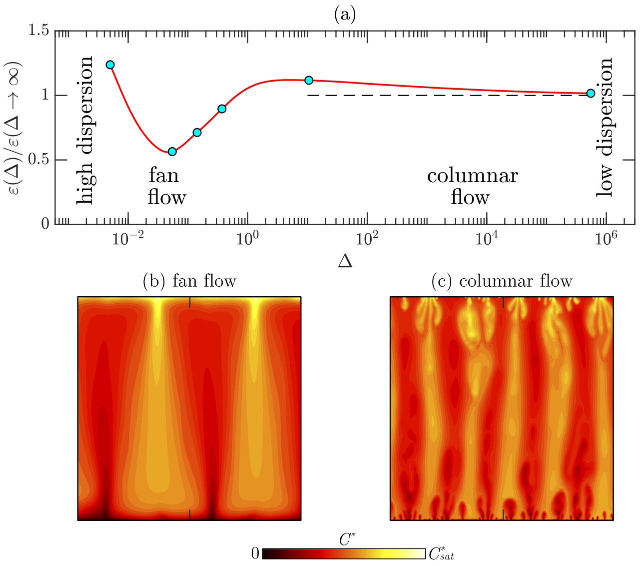

**FIG. 4.** (a) Dimensionless dissolution rate normalized by the value in the absence of dispersion, $\varepsilon(\Delta \to \infty)$. We assume $\varepsilon(\Delta \to \infty) = 10^{-5}$ (dashed line), which is attained asymptotically. The trend is obtained from direct numerical simulations,[35] assuming $Ra = 2 \times 10^4$ and $r = 10$. For $\Delta \ll 1$, dispersion makes the plumes to expand in the horizontal direction (fan flow), whereas for $\Delta \gg 1$, plumes grow vertically in a symmetric fashion (columnar flow). Bullets are used for later discussion. Concentration distribution for a porous domain with high dispersion [$\Delta \approx 10^{-2}$, panel (b)] and low dispersion [$\Delta \approx 5 \times 10^5$, panel (c)] is also shown (adapted from Ref. 35).

($\Delta \geq 1$), the width of the plumes is independent of the distance from the CO$_2$-brine interface, i.e., the plumes grow vertically in a columnar-like flow [Fig. 4(c)]. In contrast, when the effect of dispersion is increased, the solute tends to spread also horizontally, making the plumes to widen as the distance from the interface is increased [fan flow, Fig. 4(b)]. In fan flow conditions, the convective flux reduces considerably with respect to the value in the absence of dispersion [$\varepsilon(\Delta)/\varepsilon(\Delta \to \infty) \approx 0.5$ for $\Delta = 5 \times 10^{-2}$]. If dispersion is further increased ($\Delta < 5 \times 10^{-2}$), the small scales of the flow cannot be sustained anymore: the structure of the flow at the interface changes and the boundary layer thickens. As a result, the flow becomes gradually more stable and steady, and the dissolution rate increases.

In this work, we consider that the dimensionless dissolution rate $\varepsilon$ depends on $\Delta$ as prescribed by Wen, Chang, and Hesse[35] and shown in Fig. 4(a). We assume that in the absence of dispersion, the dissolution rate corresponds to that considered in isotropic domains, $\varepsilon(\Delta \to \infty) = 10^{-5}$.

## IV. RESULTS

As a result of the set of parameters considered in Sec. III ($M = M_m = 1$), the governing equations (19) and (20) reduce to the following form:

$$\frac{\partial h}{\partial t} - \frac{\partial}{\partial x}\left[(1-h)h\frac{\partial h}{\partial x} - \delta h h_m \frac{\partial h_m}{\partial x}\right] = -\varepsilon_0, \tag{26}$$

$$\frac{\partial h_m}{\partial t} - \frac{\partial}{\partial x}\left[\delta(1-h_m)h_m\frac{\partial h_m}{\partial x} - h h_m \frac{\partial h}{\partial x}\right] = \frac{\varepsilon_0}{X_v}. \tag{27}$$

We solve numerically Eqs. (26) and (27), with symmetry boundary conditions at $x = 0$. Discretization in space and time integration consist of the fourth-order finite difference scheme and second order explicit method, respectively, which have been implemented in an in-house FORTRAN solver. Grid spacing is uniform and equal to $\Delta x = 1/10$, and the time step is constant and equal to $\Delta t = 0.01$. The post-processing of the data produced has been carried out in MATLAB.

### A. Self-similar solution for the one-current model

The set of Eqs. (19) and (20) describes the evolution of the flow, which is analyzed here in terms of nose, $x_n(t)$, of the CO$_2$ current. The non-linear character of this system makes analytical solutions hard to obtain. However, predictions on the evolution of the current height, $h(t)$, can be made in the case of one-current ($h_m = 0$) and unconfined domains, i.e., when $h^* \ll H^*$ ($f = 0$). Pritchard, Woods, and Hogg[55] found that Eq. (19) has an exact similarity solution, which reads

$$h(x,t) = \frac{t^{-1/3}}{6}\left(9^{2/3} - \frac{x^2}{t^{2/3}}\right) - \frac{3}{4}\varepsilon t, \tag{28}$$

where $x \leq x_n(t)$. Therefore, one can find that the evolution of the current nose, defined as the value of $x$ in which $h(x,t) = 0$, is

$$x_n(t) = (9t)^{1/3}\sqrt{1 - \frac{\varepsilon}{18}(9t)^{4/3}}. \tag{29}$$

In the absence of dissolution ($\varepsilon = 0$), the current evolves as

$$x_n(t) = (9t)^{1/3}. \tag{30}$$

Equations (28) and (29) well describe the evolution of the CO$_2$ current also in the two-current model, provided that the current of heavy mixture and the CO$_2$ current are not in contact. We will refer to these solutions for the analysis of the early-stage evolution of the system.

We performed three sets of simulations, labeled S1, S2, and S3, in which we analyze the effect of domain size (Sec. IV B), anisotropy of the medium (Sec. IV C), and dispersion (Sec. IV D), respectively. A summary of the parameters used in the simulations is reported in Table I.

### B. Influence of domain width (S1)

We considered an isotropic porous layer ($\gamma = 1$), in the absence of dispersion ($\Delta \to \infty$), with a dimensionless dissolution rate $\varepsilon = 10^{-5}$, and we analyze the effect of the domain width ($L$) on the evolution of the flow. The domain width has an influence on both the CO$_2$ and CO$_2$ + brine currents. However, the current of the heavy mixture is more influenced by the domain width since it is typically more extended in space. The minimum domain width considered is defined as $L_{\min} = 1/X_v$, i.e., corresponding to the minimum width required to achieve a complete dissolution of the initial volume of CO$_2$ injected. The maximum value of the domain width considered, $L_\infty$, is given by the maximum extension of the CO$_2$ + brine current, which has been determined from a preliminary numerical simulation. For clarity, the behavior is shown in Fig. 5 only in correspondence with few of the values of $L$ considered.

Initially [Fig. 5(a)], the current nose $x_n(t)$ follows the evolution predicted by the one-current model [Eq. (29), dashed line], and the evolution is independent of the domain size. At $t \approx 4 \times 10^3$, the influence of the second current on the process of dissolution becomes significant. The interfacial area along which dissolution can take place is reduced. As a result, buoyancy controls the evolution of the $CO_2$ current, which spreads further horizontally along the top cap rock of the reservoir, and $x_n$ grows consequently.

At $t = 3.5 \times 10^4$, the current achieves the maximum extension ($x_n \approx 28$) and only afterward the domain width influences the dynamics of the currents. The late-stage evolution [Fig. 5(b)] is indeed very sensitive to variations of $L$. For low values of domain width, the horizontal growth of the heavy current is hindered. As a result, the current of the $CO_2$ + brine mixture will grow in height, and the portion of the interfacial area between $CO_2$ and brine will further reduce, slowing down considerably the dissolution process. However, the evolution of the current nose will be always confined between the two gray regions of the $(x, t)$ space, bounded by the extreme curves $L_{\min}$ and $L_\infty$: the brine-rich region is characterized by the absence of the $CO_2$ current, while the $CO_2$-rich region marks the portion of the $(x, t)$ space occupied by the current. This classification provides a graphical interpretation of the extension of the $CO_2$ current along the upper horizontal impermeable layer of the reservoir.

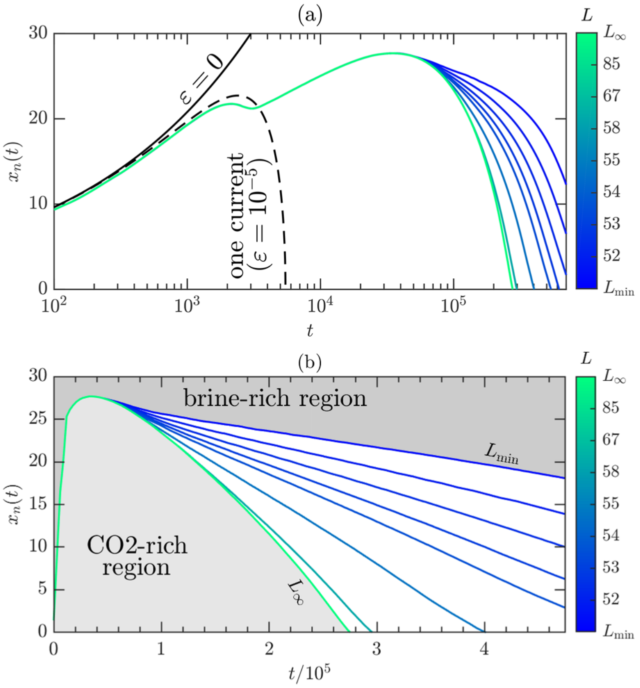

**FIG. 5.** Evolution of the current nose ($x_n$) of a buoyant $CO_2$ plume. The domain width $L$ varies within the interval $L_{\min} \le L \le L_\infty$, with $L_{\min} = 1/X_v$ (blue) and $L_\infty = 140$ (green). The values of $L$ corresponding to the curves shown are explicitly indicated in color bars. The early stage of the dissolution process (a) is independent of the domain size, whereas the long-term dynamics (b) is strongly influenced by the domain width. Note that the evolution of the systems with $L = L_\infty$ and $L = 85$ is nearly the same, and the two curves are not distinguishable. The evolution predicted by the one-current model without dissolution [Eq. (30), solid line] and with dissolution [Eq. (29), dashed line] is also shown.

### C. Influence of anisotropy (S2)

We consider now the effect of porous medium anisotropy on the evolution of the currents. These results are particularly important because of the lack of experimental data in anisotropic porous media, where only models and numerical simulations are used to study the evolution of the flow. In particular, we analyze a domain of width $L = 140$ in the absence of dispersion ($\Delta \to \infty$). The volume of $CO_2$ injected is $L_0^* H^*/\sqrt{\gamma}$, which gives a unitary dimensionless volume. We choose this configuration to have dimensionless results that can be compared with cases S1 and S3. The dissolution rate accounts for the permeability variation in the horizontal direction, i.e., $\varepsilon = \varepsilon(\gamma)$, as discussed in Sec. III B.

The time-dependent evolution of the $CO_2$ current nose ($x_n$) is shown in Fig. 6. The permeability ratio varies between $\gamma_{\min} = 1/8$ (black, strongly anisotropic) and $\gamma_{\max} = 1$ (yellow, isotropic). For clarity, $x_n(t)$ is shown in Fig. 6 only for few values of $\gamma$. We observe that the influence of anisotropy is remarkable in the initial phase of the dissolution process, where the growth of the current nose is well described by the one-current model with dissolution rate $\varepsilon(\gamma)$ [Eq. (29), dashed lines]. It is worth noting that the final stage of the mixing process is not influenced by the domain anisotropy, and no relevant change in the lifetime is observed. This observation can be explained in terms of dynamics of the currents.

Initially, the current of $CO_2$ is controlled by buoyancy, which makes the current to spread along the top boundary and, therefore, $x_n$ increases. Afterward, since the interfacial area between the currents of $CO_2$ and brine increases, dissolution dominates over buoyancy: the current nose is observed to reach a maximum (buoyancy is exactly balanced by dissolution) and then decreases

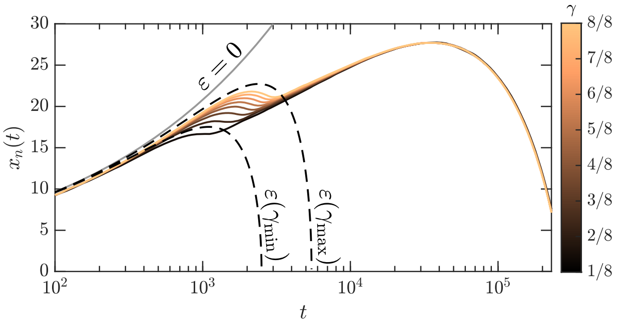

**FIG. 6.** Evolution of the current nose of a buoyant $CO_2$ plume ($x_n$). The permeability ratio $\gamma$ varies between $\gamma_{\min} = 1/8$ (black) and $\gamma_{\max} = 1$ (yellow). The values of $\gamma$ corresponding to the curves shown are explicitly indicated in the color bar. The early stage of the dissolution process is influenced by the permeability ratio, whereas the final stage is independent of $\gamma$. The evolution predicted by the one-current model with dissolution rate $\varepsilon(\gamma)$ [Eq. (29), dashed line] is shown for the minimum and maximum values of anisotropy ratio considered. The evolution of the current in the absence of dissolution [$\varepsilon = 0$, solid gray line, Eq. (30)] is also reported.

(dissolution overcomes buoyancy). The evolution of the currents is strongly conditioned by the dissolution rate $\varepsilon$, which increases with the anisotropy of the system (i.e., when $\gamma$ decreases). As a result, $x_n(t)$ grows faster in isotropic media compared to anisotropic media since the dissolution rate is lower and the effect of dissolution becomes dominant later. Afterward, the reduction in the current nose is arrested by the presence of the current of the heavy mixture, which diminishes the interfacial area between $CO_2$ and brine, considerably slowing down the dissolution process and making buoyancy again dominant. This dynamics brings to the new growth of $x_n$, a phase characterized by a tiny $CO_2$-brine interfacial area: the evolution of the currents is purely controlled by buoyancy and the dissolution rate plays no role. Buoyancy continues to make the current of $CO_2$ to expand until the $CO_2$-brine interfacial area is sufficiently large to make dissolution dominant over buoyancy again. Hereinafter ($t > 4 \times 10^4$), the reduction in the remaining volume of $CO_2$ is not balanced by the buoyant expansion of the current, and the nose reduces monotonically until the current dissolves completely. We conclude that the late stage dynamics of the currents are not influenced by the anisotropy of the medium. However, the changes observed in the early stage may bear important implications for the $CO_2$ storage process.

To investigate more in detail the effect of anisotropy on the short-term evolution of the current, we consider the volume of $CO_2$ dissolved per unit depth, $V(t)$, defined as

$$V(t) = 1 - \int_0^{x_n(t)} h(x,t)\,\mathrm{d}x. \tag{31}$$

Therefore, we have that $V(t=0) = 0$ and $V(t \to \infty) = 1$. Equation (31) can also be used to compute the volume of solute dissolved in the absence of interactions between the currents of $CO_2$ and $CO_2$ + brine (one-current model with dissolution), i.e., integration of Eq. (31) with expressions (28) and (29) gives

$$V(t) = 1 - \left[1 - \frac{\varepsilon}{18}(9t)^{4/3}\right]^{3/2}. \tag{32}$$

We wish to remark here the implications of the dimensionless set of variables used for the results presented. In all simulations considered, the initial dimensionless $CO_2$ volume is unitary. However, while the vertical domain size is made dimensionless with respect to $H^*$, the initial horizontal width of the $CO_2$ current is scaled with $L_0^*/\sqrt{\gamma}$. As a result, although the dimensionless volume of $CO_2$ injected is always 1, it corresponds to different physical volumes, which depend on the permeability ratio. The evolution predicted by the one-current model for the two extreme cases ($\gamma_{\min} = 1/8$ and $\gamma_{\max} = 1$) is reported in Fig. 7. Low values of permeability ratio, corresponding to the high value of the dissolution rate $\varepsilon(\gamma)$, produce a favorable dissolution scenario: when $\gamma = \gamma_{\min}$, the time required to dissolve 30% of the volume of $CO_2$ initially injected is much smaller (about 50%) with respect to the isotropic case ($\gamma = \gamma_{\max}$). In other terms, the short-term dissolution efficiency is higher when the medium is anisotropic. On the other hand, the influence of $\gamma$ is negligible for the long-term dissolution dynamics.

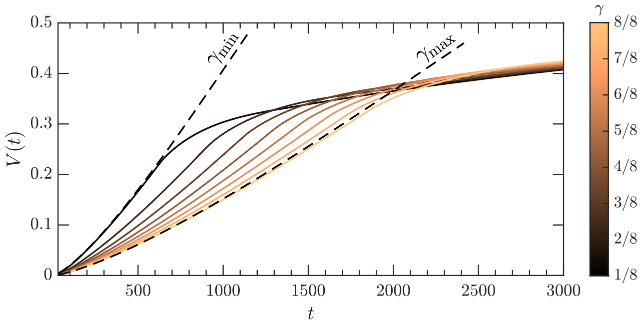

**FIG. 7.** Dimensionless volume of $CO_2$ per unit depth dissolved for the range of permeability ratio considered, $\gamma_{\min} \leq \gamma \leq \gamma_{\max}$, with $\gamma_{\min} = 1/8$ (black) and $\gamma_{\max} = 1$ (yellow). The one-current model predictions in correspondence with $\varepsilon(\gamma_{\min})$ and $\varepsilon(\gamma_{\max})$ [Eq. (32), dashed lines] are also shown. The values of $\gamma$ corresponding to the curves shown are explicitly indicated in the color bar.

## D. Influence of dispersion (S3)

As discussed in Sec. III B, we investigate the effect of dispersion by varying the dimensionless dissolution rate ($\varepsilon$) as a function of $\Delta$, which measures the relative importance of molecular diffusion to transverse dispersion. We show in Fig. 4(a) that the dissolution parameter varies in a non-monotonic way with respect to $\Delta$. The flow dynamics is briefly recalled here. When $\Delta \geq 1$, convection dominates over dispersion, and the width of the plumes is independent of the distance from the $CO_2$-brine interface, i.e., the plumes grow vertically in a columnar-like flow. In contrast, when $\Delta$ reduces, i.e., the effect of transverse dispersion is increased, the solute spreads in perpendicular direction with respect to the main flow direction, and the flow structure evolves toward a fan flow. The convective flux reduces considerably ($\approx 50\%$ for $\Delta = 5 \times 10^{-2}$) with respect to the value in the absence of dispersion ($\Delta \to \infty$). If the effect of dispersion is further increased ($\Delta < 5 \times 10^{-2}$), the flow changes completely. Small interfacial plumes do not form anymore, the thickness of the boundary layer increases and the flow becomes steady, with a corresponding increase in the dissolution rate.

To analyze the effect of dispersion, we considered isotropic domains with constant width, $L = 140$. We performed simulations for $5 \times 10^{-3} < \Delta < 5 \times 10^5$. The results are presented in terms of volume of $CO_2$ dissolved. We report the evolution of $V$ in Fig. 8 for some representative values of $\Delta$, indicated with bullets in Fig. 4(a). The volume dissolved is computed as in Eq. (31) and only the early stage dynamics is shown ($t \leq 10^4$) in Fig. 8(a) since for $t > 4 \times 10^3$, the difference among the different dispersion coefficients considered is negligible. Initially, the dynamics is very sensitive to the value of dissolution, and therefore of $\Delta$, and the flow evolves following the one-current model prediction, shown as dashed lines in Fig. 8(a) [obtained assuming $\varepsilon = \varepsilon(\Delta)$ in Eq. (32)]. The self-similar behavior exhibited in the early stage is even more apparent when time is rescaled by $[\varepsilon(\Delta)/\varepsilon(\Delta \to \infty)]^{3/4}$ [Fig. 8(b)]. In this stage, the flow consists of two currents not in contact. Dissolution can take place along the entire interface of the buoyant current, and the rate at which $CO_2$ dissolves is roughly steady (nearly constant slope of the curves).

After the initial phase in which the current of $CO_2$ is purely controlled by buoyancy and dissolution, the effect of the second current comes into play. When $t \times [\varepsilon(\Delta)/\varepsilon(\Delta \to \infty)]^{3/4} \approx 1700$, the rate at which the $CO_2$ dissolves reduces. The slope of the curves in Fig. 8(b) changes, and this marks the time at which the current of the

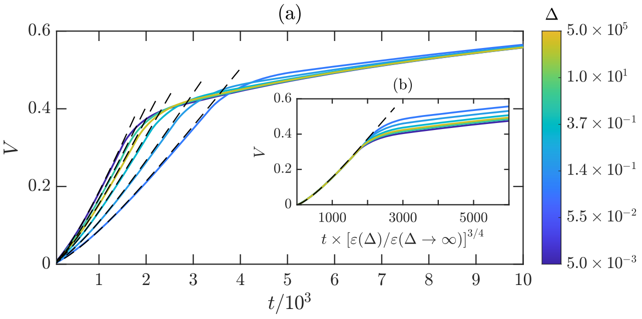

**FIG. 8.** (a) Dimensionless volume of $CO_2$ per unit depth dissolved in time for the range of $\Delta$ considered. The one-current model predictions in correspondence with each $\varepsilon(\Delta)$ [Eq. (32), dashed lines] are also shown. (b) When time is rescaled with $\varepsilon(\Delta)/\varepsilon(\Delta \to \infty)$, the profiles exhibit a self-similar evolution in the initial phase of the migration process. The dashed line represents Eq. (32) with $\varepsilon(\Delta \to \infty)$. The values of $\varepsilon(\Delta)$ and $\Delta$ corresponding to the simulations shown, explicitly reported in the color bar, are also indicated with bullets in Fig. 4(a).

heavy mixture touches the current of $CO_2$. As a result, dissolution is inhibited along the interfacial area between the currents of $CO_2$ and $CO_2$ + brine mixture. Buoyancy becomes again dominant over dissolution, and the current of $CO_2$ spreads further horizontally. For $t > 10^4$ (not shown), the behavior is the same for all $\Delta$ considered: dissolution can still take place along the small portion of the interface of buoyant current in contact with brine, and the complete dissolution is achieved at $t \approx 2.5 \times 10^5$ (for all $\Delta$ considered).

We conclude that the effect of transverse dispersion, similar to that observed for anisotropy, may bear implications for the initial phase of the dissolution process. In particular, the lifetime and maximum spread of the current are not influenced by dispersion. However, the early stage of the migration process, analyzed here in terms of volume of $CO_2$ dissolved in time, is sensitive to the transverse dispersion and may influence in a positive or negative manner the short-term efficiency of the storage process. If $\Delta < 10^{-2}$, the dissolution rate is higher than in the absence of dispersion ($\Delta \to \infty$), and the time required to dissolve a fixed amount of solute reduces with respect to the case with no transverse dispersion. In contrast, when $10^{-2} < \Delta < 10^1$, the dissolution rate can drop to 50% of the case with $\Delta \to \infty$ [see Fig. 4(a)], influencing negatively the dissolution (and safe storage) of $CO_2$.

## V. DISCUSSION AND CONCLUSIONS

We analyze the evolution of a migrating current of $CO_2$ in saline aquifers in the frame of carbon sequestration processes. After injection, $CO_2$ is buoyant and tends to spread below the upper cap rock, increasing the risk of escaping to reach the upper layers of the aquifer. However, the mixture that forms from the dissolution of $CO_2$ in brine is denser than both $CO_2$ and brine and sinks down, making the storage process effective. The evolution of this system is made complicated by the interaction of the buoyant current of $CO_2$ and the current of $CO_2$ + brine. In this work, we used a large-scale model to investigate the effect of reservoir properties on the evolution of the currents. In particular, the contribution of this work consists of including additional physical effects to the model proposed by MacMinn *et al.*[6] and also evaluating the results in the context of carbon sequestration. We considered the effect of three different physical properties, namely, domain width ($L$), anisotropy of the medium ($\gamma$, defined as the ratio of vertical-to-horizontal permeability), and dispersion of the porous matrix, quantified with $\Delta$ (the relative importance of molecular diffusion to transverse dispersion).

We considered the case study of the Frio C Formation (Texas, US), characterized by vertical permeability $k_v = 2.5 \times 10^{-12}$ m$^2$, porosity $\phi = 0.3$, and layer height $H^* = 7$ m. Other well-studied aquifers (e.g., the Sleipner Site, North Sea) have similar properties, and the results presented here can be extended to those cases as well. However, the situation can potentially be very different when the permeability is changed (see Table II): large values of permeability (e.g., the Alberta Basin, Canada) correspond to favorable scenarios, in which the dissolution process is more efficient, since the vertical solute flux is proportional to the buoyancy velocity. In contrast, the safety of the storage process in sites characterized by lower values of permeability (e.g., the Bravo S1 Dome, NM, US) is lower.

First, we analyzed the influence of domain size. We consider domains of different widths from the minimum size required to achieve a complete dissolution of the volume of $CO_2$ injected to an infinite domain width. This analysis is motivated by the fact that reservoirs identified as possible sequestration sites can hardly be considered as flat and infinitely extended layers, e.g., due to the presence of inclined walls or irregularities of the layer shape. We found that the horizontal confinement of the reservoir blocks the horizontal growth of the heavy current, making it grow vertically. As a result, the $CO_2$-brine interfacial area reduces further with respect to unconfined domains, promoting the horizontal expansion of the buoyant current. We observe (Fig. 9) that for widths $L^* \geq 1$ km, the lifetime of the current (i.e., the time required to dissolve 99% of the volume of $CO_2$ initially injected), $t^*_{\mathrm{end}}$, does not vary (≈ 900 years), whereas it may considerably increase when the domain size in lowered. We conclude that the efficiency of the trapping mechanism is remarkably reduced when the horizontal extension of the layer is

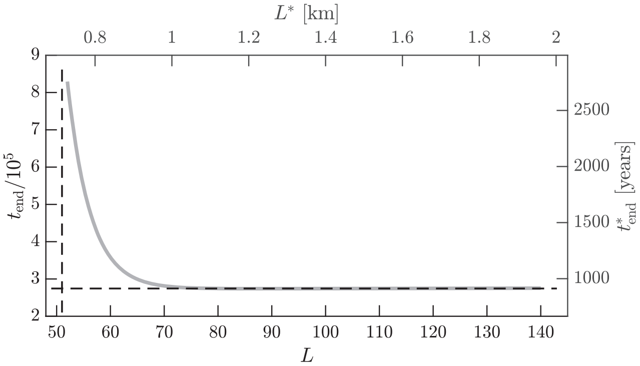

**FIG. 9.** Current lifetime in correspondence with different domain widths. Left and bottom axes: dimensionless lifetime, $t_{\mathrm{end}}$, and domain width, $L$. Top and right axes: dimensional lifetime, $t^*_{\mathrm{end}}$, and domain width, $L^*$. The minimum domain size required to achieve a complete dissolution of the volume of $CO_2$ injected ($L_{\mathrm{min}} = 51$, corresponding to $L^*_{\mathrm{min}} \approx 700$ m) is indicated by the vertical dashed line. The lifetime of the current obtained for $L \geq L_\infty = 140$, corresponding to $L^* \geq L^*_\infty \approx 2$ km, is represented by the horizontal dashed line.

lower than 1 km. These results also show that accurate numerical simulations at the Darcy scale in such large domains are beyond the current computational resources, and large-scale models should be used.

We analyze then the effect of the anisotropy of the medium, characterized here by the ratio of vertical-to-horizontal permeability, $\gamma = k_v/k_h$. In particular, we consider a domain with constant width and vary the horizontal permeability, maintaining the vertical permeability constant. In this way, we can compare systems characterized by different media but the same vertical driving force, i.e., the same buoyancy velocity. The horizontal component ($k_h$) is set to be $k_h \geq k_v$, which gives $0 \leq \gamma \leq 1$. As a result, the more the media are anisotropic (i.e., the smaller the $\gamma$), the lower the hydrodynamic horizontal flow resistance is. Due to continuity, this will produce an increase in the vertical flow velocity and the dissolution rate. We included the effect of anisotropy modeling the dissolution rate, which is defined as a function of $\gamma$. We observed that the long-term effect of anisotropy is negligible, i.e., the lifetime of the current is not influenced by $\gamma$. However, anisotropy may produce beneficial effects on the short-term dissolution dynamics, when the buoyant current is only controlled by buoyancy and dissolution, and the heavy current is not sufficiently developed in the vertical direction to inhibit dissolution. The time $t_\sigma$ taken to dissolve a fraction $\sigma$ of the initial volume of $CO_2$ injected is very sensitive to the anisotropy ratio. For instance, the time required to dissolve 20% of the initial volume of $CO_2$ injected (Fig. 10) is of about 4 years for isotropic porous media ($\gamma = 1$), whereas it drops to 2 years in anisotropic porous media with $\gamma = 1/8$.

When a fluid flows through a porous medium, it follows sinuous paths, which makes the transported solute ($CO_2$ in this case) to spread further. This effect is defined as dispersion and is quantified here with $\Delta$ (the relative importance of molecular diffusion to transverse dispersion). Dispersion influences considerably the dissolution rate of $CO_2$ in brine, and we included this effect in the large-scale model defining the dissolution rate as a function of $\Delta$. To this aim, we used the results of accurate Darcy simulations[35] that clearly linked the dissolution rate to the structure of the flow. The time $t_\sigma$ required to dissolve a fixed portion $\sigma$ of solute is shown as a function of $\Delta$ in Fig. 11. When $\Delta > 10$, the effect of dispersion is overcome by convection. The flow structure is columnar, and the dissolution rate tends asymptotically to the value obtained for isotropic reservoirs in the absence of dispersion (dashed lines in Fig. 11). When $\Delta < 10^{-2}$, dispersion dominates over molecular diffusion, the small-scale structures are smoothed, and the flow is steady. Dispersion produces lateral spreading of the plumes (fan flow), and the dissolution rate is higher than in the absence of dispersion ($\Delta \to \infty$). As a result, $t_\sigma$ is lower than in the absence of dispersion, corresponding to a beneficial effect for the storage process. In contrast, for intermediate values of $\Delta$ (i.e., $10^{-2} < \Delta < 10^1$), the transition from columnar to fan flow makes the dissolution drop up to 50% of the case with $\Delta \to \infty$. In this case, the influence of dispersion on the storage of $CO_2$ is negative, e.g., $t_{20\%}$ can increase from 4 years (no dispersion) to 6 years ($\Delta = 5 \times 10^{-2}$). To conclude, the early stage of the migration process, analyzed here in terms of $t_\sigma$, is sensitive to the transverse dispersion and may influence in a positive or negative manner the short-term efficiency of the storage process. The effect of transverse dispersion, similar to that observed for the anisotropy, influences the dynamics before the contact of the heavy current with the buoyant current, and it has no remarkable effect on the lifetime and maximum spread (maximum of the current nose).

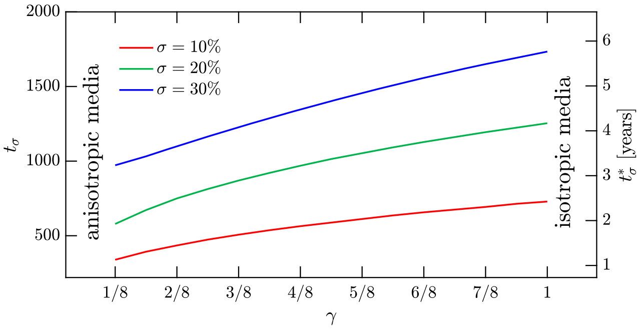

**FIG. 10.** Effect of anisotropy $\gamma$ on $t_\sigma$, i.e., the time required to dissolve a fraction $\sigma$ of the initial volume of $CO_2$ injected. Left axis: dimensionless value of $t_\sigma$. Right axis: dimensional value of $t^*_\sigma$. The effect of anisotropy is considerable, e.g., $t^*_{20\%}$ in isotropic ($\gamma = 1$) reservoirs (≈ 4 years) is doubled with respect to domains with anisotropy ratio $\gamma = 1/8$ (≈ 2 years).

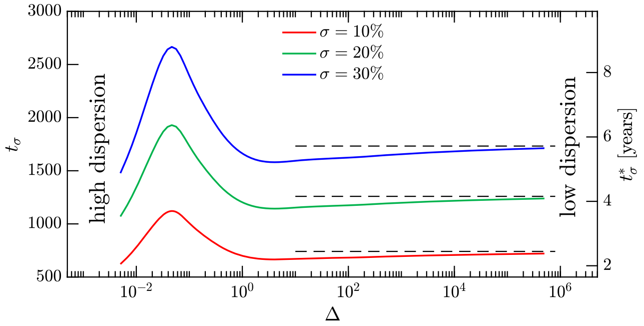

**FIG. 11.** Effect of transverse dispersion ($\Delta$) on the time $t_\sigma$, i.e., the time required to dissolve a fraction $\sigma$ of the initial volume of $CO_2$ injected. For formations with low dispersion ($\Delta > 10^5$), $t_\sigma$ tends asymptotically to the value measured in isotropic domains in the absence of dispersion (see Fig. 10, $\gamma = 1$), represented here by dashed lines. In domain with high dispersion ($\Delta < 10^{-2}$), the dissolution is more efficient than in the absence of dispersion. For intermediate values of dispersion ($10^{-2} < \Delta < 10^1$), the dissolution rate can drop to 50% of the case with $\Delta \to \infty$, and $t_\sigma$ increases considerably.

The results reported in this work are relative to the set of parameters used, and the behavior may significantly change with a different combination of porous media and fluid properties. However, this model represents a key tool to quantify the large-scale and long-term dynamics of gravity currents, which can hardly be predicted by accurate numerical simulations at the Darcy scale. A further advantage of the presented approach consists of the possibility of accounting for different flow features, such as anisotropy and dispersion. The configuration considered consists of a simplified model of a geological formation, which may be characterized by the presence of inclined boundaries,[56,57] heterogeneities,[25,28,29] rock dissolution,[58,59] and chemical reactions.[60,61] If properly parametrized (e.g., in terms of dissolution rate), these effects can also be included in the

**TABLE II.** Porous properties (permeability $k$, porosity $\phi$, and layer thickness $H^*$) of geological formations identified as possible sequestration sites.

| Reference | Site name | Location | $k$ ($10^{-12}$ m$^2$) | $\phi$ | $H$ (M) |
|---|---|---|---|---|---|
| 63 | Alberta Basin S1 | Western Canada | 14.0 | 0.06 | 10 |
| 63 | Alberta Basin S4 | Western Canada | 16.0 | 0.07 | 10 |
| 63 | Alberta Basin S11 | Western Canada | 32 | 0.12 | 13 |
| 63 | Alberta Basin S21 | Western Canada | 66 | 0.22 | 40 |
| 63 | Alberta Basin S24 | Western Canada | 135 | 0.09 | 60 |
| 12 | Nagaoka | Japan | 0.0069 | 0.23 | 12 |
| 48 | In Salah | Algeria | 0.01 | 0.15 | 20 |
| 48 | Frio C Formation | Texas | 2 | 0.30 | 7 |
| 64 | Bravo S1 | New Mexico | 0.002 | 0.14 | 130 |
| 33 | Bravo S2 | New Mexico | 0.987 | 0.37 | 25 |
| 48 | Sleipner S1 | North Sea | 2 | 0.35 | 20 |
| 33 | Sleipner S2 | North Sea | 2 | 0.09 | 50 |
| 65 | Sleipner S8 | North Sea | 4 | 0.03 | $\geq 5$ |

**TABLE III.** Fluid properties (density, $\rho$, and viscosity, $\mu$) estimated at the injection depth for the fluids considered ($CO_2$, $c$; brine, $w$; and $CO_2$ + brine mixture, $m$). We assumed that the viscosity of brine and $CO_2$ + brine mixture matches.

| Reference | $\mu_c$ (mPa s) | $\mu_w$ (mPa s) | $\rho_c$ (kg/m$^3$) | $\rho_w$ (kg/m$^3$) | $\Delta\rho_m$ (kg/m$^3$) |
|---|---|---|---|---|---|
| 65 | 0.03–0.05 | | 420–610 | 1020 | |
| 52 | 0.02–0.06 | 0.20–1.58 | 266–733 | 945–1230 | |
| 33 | | 0.52–1.32 | | | 2.4–8.8 |
| 53 | | 0.59 | | 994 | 10.5 |

present model. Motivated by the injection scenario consisting of a linear array of wells, we considered a two-dimensional planar flow. The three-dimensional character of the flow may become important at later times as plumes migrate sufficiently far from the injection point. However, the present model can be adapted, with minor modifications, to three-dimensional axisymmetric geometries, more representative of isolated injection wells.

## ACKNOWLEDGMENTS

Professor C. W. MacMinn is gratefully acknowledged for comments provided on the early draft of this manuscript. The author would like to acknowledge the financial support from Project No. 2015-1-IT02-K103-013256 funded by EC Erasmus+. Dr. Baole Wen is acknowledged for providing the data of Fig. 4. The anonymous reviewers, whose comments and suggestions helped to improve this manuscript, are also acknowledged.

## APPENDIX A: PHYSICAL PROPERTIES OF FORMATIONS AND FLUIDS

We report here the parameters for a set of representative and well-studied geological formations identified as possible sequestration sites. In Table II, we focus on the domain properties, and we indicate permeability ($k$), porosity ($\phi$), and layer thickness ($H^*$). The parameters vary over a wide range also within the same site when different layers are considered.

In Table III, we report the fluid properties (density $\rho$ and viscosity $\mu$) for different formation types (e.g., "deep" or "shallow" and "cold" or "warm"[52]). In this case, the fluid properties vary over a wide range of values. The depth at which the formations are located plays a key role in the determination of the thermophysical properties of the fluids; therefore, it is not possible to provide a unique set of parameters representative of all geological formations. Correlations to compute the properties of $CO_2$–brine mixtures as a function of pressure and temperature were provided by Hassanzadeh *et al.*[62]

## DATA AVAILABILITY

The data that support the findings of this study are available from the author upon reasonable request.

## REFERENCES

[1] B. Netz, O. Davidson, P. Bosch, R. Dave, L. Meyer *et al.*, Climate change 2007: Mitigation, Contribution of working group III to the fourth assessment report of the intergovernmental panel on climate change, Summary for policymakers, 2007.

[2] D. P. Schrag, "Preparing to capture carbon," Science **315**, 812–813 (2007).

[3] S. J. Friedmann, "Geological carbon dioxide sequestration," Elements **3**, 179–184 (2007).

[4]M. L. Szulczewski, C. W. MacMinn, H. J. Herzog, and R. Juanes, "Lifetime of carbon capture and storage as a climate-change mitigation technology," Proc. Natl. Acad. Sci. U. S. A. **109**, 5185–5189 (2012).

[5]H. Emami-Meybodi, H. Hassanzadeh, C. P. Green, and J. Ennis-King, "Convective dissolution of $CO_2$ in saline aquifers: Progress in modeling and experiments," Int. J. Greenhouse Gas Control **40**, 238–266 (2015).

[6]C. W. MacMinn, J. A. Neufeld, M. A. Hesse, and H. E. Huppert, "Spreading and convective dissolution of carbon dioxide in vertically confined, horizontal aquifers," Water Resour. Res. **48**, W11516, https://doi.org/10.1029/2012wr012286 (2012).

[7]C. W. MacMinn and R. Juanes, "Buoyant currents arrested by convective dissolution," Geophys. Res. Lett. **40**, 2017–2022, https://doi.org/10.1002/grl.50473 (2013).

[8]H. E. Huppert and J. A. Neufeld, "The fluid mechanics of carbon dioxide sequestration," Ann. Rev. Fluid Mech. **46**, 255–272 (2014).

[9]J. A. Neufeld and H. E. Huppert, "Modelling carbon dioxide sequestration in layered strata," J. Fluid Mech. **625**, 353–370 (2009).

[10]A. C. Slim, "Solutal-convection regimes in a two-dimensional porous medium," J. Fluid Mech. **741**, 461–491 (2014).

[11]X. Xu, S. Chen, and D. Zhang, "Convective stability analysis of the long-term storage of carbon dioxide in deep saline aquifers," Adv. Water Res. **29**, 397–407 (2006).

[12]T. Nakajima, T. Ito, and Z. Xue, "Numerical simulation of the $CO_2$ behavior to obtain a detailed site characterization: A case study at Nagaoka pilot-scale injection site," Energy Proc. **114**, 2819–2826 (2017) [13th International Conference on Greenhouse Gas Control Technologies, GHGT-13, 14–18 November 2016, Lausanne, Switzerland].

[13]D. R. Hewitt, J. A. Neufeld, and J. R. Lister, "Convective shutdown in a porous medium at high Rayleigh number," J. Fluid Mech. **719**, 551–586 (2013).

[14]M. De Paoli, F. Zonta, and A. Soldati, "Dissolution in anisotropic porous media: Modelling convection regimes from onset to shutdown," Phys. Fluids **29**, 026601 (2017) (1994-present).

[15]J. J. Hidalgo, J. Fe, L. Cueto-Felgueroso, and R. Juanes, "Scaling of convective mixing in porous media," Phys. Rev. Lett. **109**, 264503 (2012).

[16]J. J. Hidalgo, M. Dentz, Y. Cabeza, and J. Carrera, "Dissolution patterns and mixing dynamics in unstable reactive flow," Geophys. Res. Lett. **42**, 6357–6364, https://doi.org/10.1002/2015gl065036 (2015).

[17]M. De Paoli, V. Giurgiu, F. Zonta, and A. Soldati, "Universal behavior of scalar dissipation rate in confined porous media," Phys. Rev. Fluids **4**, 101501 (2019).

[18]M. Alipour, M. De Paoli, and A. Soldati, "Concentration-based velocity reconstruction in convective Hele–Shaw flows," Exp. Fluids **61**, 195 (2020).

[19]J. A. Neufeld, M. A. Hesse, A. Riaz, M. A. Hallworth, H. A. Tchelepi, and H. E. Huppert, "Convective dissolution of carbon dioxide in saline aquifers," Geophys. Res. Lett. **37**, L22404, https://doi.org/10.1029/2010gl044728 (2010).

[20]R. Farajzadeh, B. Meulenbroek, D. Daniel, A. Riaz, and J. Bruining, "An empirical theory for gravitationally unstable flow in porous media," Comput. Geosci. **17**, 515–527 (2013).

[21]P. A. Tsai, K. Riesing, and H. A. Stone, "Density-driven convection enhanced by an inclined boundary: Implications for geological $CO_2$ storage," Phys. Rev. E **87**, 011003 (2013).

[22]S. Backhaus, K. Turitsyn, and R. Ecke, "Convective instability and mass transport of diffusion layers in a Hele-Shaw geometry," Phys. Rev. Lett. **106**, 104501 (2011).

[23]M. De Paoli, M. Alipour, and A. Soldati, "How non-Darcy effects influence scaling laws in Hele-Shaw convection experiments," J. Fluid Mech. **892**, A41 (2020).

[24]Y. Liang, B. Wen, M. A. Hesse, and D. DiCarlo, "Effect of dispersion on solutal convection in porous media," Geophys. Res. Lett. **45**, 9690–9698, https://doi.org/10.1029/2018gl079849 (2018).

[25]C. P. Green and J. Ennis-King, "Steady dissolution rate due to convective mixing in anisotropic porous media," Adv. Water Res. **73**, 65–73 (2014).

[26]M. De Paoli, F. Zonta, and A. Soldati, "Influence of anisotropic permeability on convection in porous media: Implications for geological $CO_2$ sequestration," Phys. Fluids **28**, 056601 (2016) (1994-present).

[27]C. Green and J. Ennis-King, "Steady flux regime during convective mixing in three-dimensional heterogeneous porous media," Fluids **3**, 58 (2018).

[28]Q. Li, W. H. Cai, B. X. Li, and C.-Y. Chen, "Numerical study of density-driven convection in laminated heterogeneous porous media," J. Mech. **36**, 665–673 (2020).

[29]E. Lindeberg and D. Wessel-Berg, "Upscaling studies of diffusion induced convection in homogeneous and heterogeneous aquifers," Energy Proc. **4**, 3927–3934 (2011).

[30]D. R. Hewitt, "Vigorous convection in porous media," Proc. R. Soc. A **476**, 20200111 (2020).

[31]A. J. Landman and R. J. Schotting, "Heat and brine transport in porous media: The Oberbeck-Boussinesq approximation revisited," Transp. Porous Media **70**, 355–373 (2007).

[32]J. J. Hidalgo and J. Carrera, "Effect of dispersion on the onset of convection during $CO_2$ sequestration," J. Fluid Mech. **640**, 441–452 (2009).

[33]H. Emami-Meybodi, "Stability analysis of dissolution-driven convection in porous media," Phys. Fluids **29**, 014102 (2017).

[34]K. Ghesmat, H. Hassanzadeh, and J. Abedi, "The effect of anisotropic dispersion on the convective mixing in long-term $CO_2$ storage in saline aquifers," AIChE J. **57**, 561–570 (2011).

[35]B. Wen, K. W. Chang, and M. A. Hesse, "Rayleigh-Darcy convection with hydrodynamic dispersion," Phys. Rev. Fluids **3**, 123801 (2018).

[36]A. Woods, *Flow in Porous Rocks: Energy and Environmental Applications* (Cambridge University Press, 2014).

[37]J. A. Letelier, N. Mujica, and J. H. Ortega, "Perturbative corrections for the scaling of heat transport in a Hele-Shaw geometry and its application to geological vertical fractures," J. Fluid Mech. **864**, 746–767 (2019).

[38]S. Gasow, Z. Lin, H. C. Zhang, A. V. Kuznetsov, M. Avila, and Y. Jin, "Effects of pore scale on the macroscopic properties of natural convection in porous media," J. Fluid Mech. **891**, A25 (2020).

[39]G. Sardina, L. Brandt, G. Boffetta, and A. Mazzino, "Buoyancy-driven flow through a bed of solid particles produces a new form of Rayleigh-Taylor turbulence," Phys. Rev. Lett. **121**, 224501 (2018).

[40]I. Ataei-Dadavi, N. Rounaghi, M. Chakkingal, S. Kenjeres, C. R. Kleijn, and M. J. Tummers, "An experimental study of flow and heat transfer in a differentially side heated cavity filled with coarse porous media," Int. J. Heat Mass Transfer **143**, 118591 (2019).

[41]M. Chakkingal, S. Kenjereš, I. Ataei-Dadavi, M. J. Tummers, and C. R. Kleijn, "Numerical analysis of natural convection with conjugate heat transfer in coarse-grained porous media," Int. J. Heat Fluid Flow **77**, 48–60 (2019).

[42]S. Liu, L. Jiang, K. L. Chong, X. Zhu, Z.-H. Wan, R. Verzicco, R. J. A. M. Stevens, D. Lohse, and C. Sun, "From Rayleigh-Bénard convection to porous-media convection: How porosity affects heat transfer and flow structure," J. Fluid Mech. **895**, A18 (2020).

[43]R. Feixiong, A. Kuznetsov, and Y. Jin, "Numerical modeling of momentum dispersion in porous media based on the pore scale prevalence hypothesis," Transpm. Porous Media **133**, 271–292 (2020).

[44]S. Gasda, J. Nordbotten, and M. Celia, "Vertically averaged approaches for $CO_2$ migration with solubility trapping," Water Resour. Res. **47**, W05528, https://doi.org/10.1029/2010wr009075 (2011).

[45]C. W. MacMinn, M. L. Szulczewski, and R. Juanes, "$CO_2$ migration in saline aquifers. Part 2. Capillary and solubility trapping," J. Fluid Mech. **688**, 321–351 (2011).

[46]J. Bear, *Dynamics of Fluids in Porous Media* (Courier Corporation, 2013).

[47]H. E. Huppert and A. W. Woods, "Gravity-driven flows in porous layers," J. Fluid Mech. **292**, 55–69 (1995).

[48]M. A. Celia, S. Bachu, J. M. Nordbotten, and K. W. Bandilla, "Status of $CO_2$ storage in deep saline aquifers with emphasis on modeling approaches and practical simulations," Water Resour. Res. **51**, 6846–6892, https://doi.org/10.1002/2015wr017609 (2015).

[49]R. Arts, O. Eiken, A. Chadwick, P. Zweigel, L. Van der Meer, and B. Zinszner, "Monitoring of $CO_2$ injected at Sleipner using time lapse seismic data," in *6th International Conference on Greenhouse Gas Control Technologies* (Elsevier, 2003), pp. 347–352.

[50] R. A. Chadwick, R. Arts, O. Eiken, G. A. Kirby, E. Lindeberg, and P. Zweigel, "4D seismic imaging of an injected $CO_2$ plume at the sleipner field, central North Sea," Geol. Soc. London Mem. **29**, 311–320 (2004).

[51] P. Zweigel, R. Arts, A. E. Lothe, and E. B. G. Lindeberg, "Reservoir geology of the Utsira Formation at the first industrial-scale underground $CO_2$ storage site (Sleipner area, North Sea)," Geol. Soc. London, Spec. Publ. **233**, 165–180 (2004).

[52] J. M. Nordbotten, M. A. Celia, and S. Bachu, "Injection and storage of $CO_2$ in deep saline aquifers: Analytical solution for CO2 plume evolution during injection," Transp. Porous Media **58**, 339–360 (2005).

[53] G. S. H. Pau, J. B. Bell, K. Pruess, A. S. Almgren, M. J. Lijewski, and K. Zhang, "High-resolution simulation and characterization of density-driven flow in $CO_2$ storage in saline aquifers," Adv. Water Res. **33**, 443–455 (2010).

[54] S. S. Pegler, H. E. Huppert, and J. A. Neufeld, "Fluid injection into a confined porous layer," J. Fluid Mech. **745**, 592–620 (2014).

[55] D. Pritchard, A. W. Woods, and A. J. Hogg, "On the slow draining of a gravity current moving through a layered permeable medium," J. Fluid Mech. **444**, 23–47 (2001).

[56] C. W. MacMinn, M. L. Szulczewski, and R. Juanes, "$CO_2$ migration in saline aquifers. Part 1. Capillary trapping under slope and groundwater flow," J. Fluid Mech. **662**, 329–351 (2010).

[57] F. J. Guerrero, R. M. Prol-Ledesma, and N. Karimi, "Transient thermo-solutal convection in a tilted porous enclosure heated from below and salted from above," Int. Commun. Heat Mass **118**, 104875 (2020).

[58] X. Fu, L. Cueto-Felgueroso, D. Bolster, and R. Juanes, "Rock dissolution patterns and geochemical shutdown of $CO_2$-brine-carbonate reactions during convective mixing in porous media," J. Fluid Mech. **764**, 296–315 (2015).

[59] M. Bickle, N. Kampman, H. Chapman, C. Ballentine, B. Dubacq, A. Galy, T. Sirikitputtisak, O. Warr, M. Wigley, and Z. Zhou, "Rapid reactions between $CO_2$, brine and silicate minerals during geological carbon storage: Modelling based on a field $CO_2$ injection experiment," Chem. Geol. **468**, 17–31 (2017).

[60] V. Loodts, C. Thomas, L. Rongy, and A. De Wit, "Control of convective dissolution by chemical reactions: General classification and application to $CO_2$ dissolution in reactive aqueous solutions," Phys. Rev. Lett. **113**, 114501 (2014).

[61] A. De Wit, "Chemo-hydrodynamic patterns and instabilities," Ann. Rev. Fluid Mech. **52**, 531–555 (2020).

[62] H. Hassanzadeh, M. Pooladi-Darvish, A. M. Elsharkawy, D. W. Keith, and Y. Leonenko, "Predicting PVT data for $CO_2$-brine mixtures for black-oil simulation of $CO_2$ geological storage," Int. J. Greenhouse Gas Control **2**, 65–77 (2008).

[63] S. Bachu, J. M. Nordbotten, and M. A. Celia, "Evaluation of the spread of acid-gas plumes injected in deep saline aquifers in western Canada as an analogue for $CO_2$ injection into continental sedimentary basins," in *Greenhouse Gas Control Technologies 7*, edited by E. Rubin, D. Keith, C. Gilboy, M. Wilson, T. Morris, J. Gale, and K. Thambimuthu (Elsevier Science, Ltd., Oxford, 2005), pp. 479–487.

[64] B. Wen, D. Akhbari, L. Zhang, and M. A. Hesse, "Convective carbon dioxide dissolution in a closed porous medium at low pressure," J. Fluid Mech. **854**, 56–87 (2018).

[65] M. Bickle, A. Chadwick, H. E. Huppert, M. Hallworth, and S. Lyle, "Modelling carbon dioxide accumulation at Sleipner: Implications for underground carbon storage," Earth Planet Soc. Lett. **255**, 164–176 (2007).